AGU PUBLICATIONS

JGR

Journal of Geophysical Research: Oceans

RESEARCH ARTICLE

10.1002/2016JC012235

Key Points:

- Diapycnal mixing is stronger in the eastern half of the Archipelago
- Elevated mixing is concentrated near sills and constrictions
- Averaged diapycnal buoyancy fluxes at depth can reach a magnitude similar to that of surface buoyancy exchange

Correspondence to:
K. G. Hughes,
hugke729@uvic.ca

Citation:
Hughes, K. G., J. M. Klymak, X. Hu, and P. G. Myers (2017), Water mass modification and mixing rates in a 1/12° simulation of the Canadian Arctic Archipelago, *J. Geophys. Res. Oceans*, *122*, 803–820, doi:10.1002/2016JC012235.

Received 11 AUG 2016
Accepted 8 DEC 2017
Accepted article online 4 JAN 2017
Published online 1 FEB 2017

Water mass modification and mixing rates in a 1/12° simulation of the Canadian Arctic Archipelago

Kenneth G. Hughes[1], Jody M. Klymak[1], Xianmin Hu[2], and Paul G. Myers[2]

[1]School of Earth and Ocean Sciences, University of Victoria, Victoria, British Columbia, Canada, [2]Department of Earth and Atmospheric Sciences, University of Alberta, Edmonton, Alberta, Canada

Abstract Strong spatial differences in diapycnal mixing across the Canadian Arctic Archipelago are diagnosed in a 1/12° basin-scale model. Changes in mass flux between water flowing into or out of several regions are analyzed using a volume-integrated advection–diffusion equation, and focus is given to denser water, the direct advective flux of which is mediated by sills. The unknown in the mass budget, mixing strength, is a quantity seldom explored in other studies of the Archipelago, which typically focus on fluxes. Regionally averaged diapycnal diffusivities and buoyancy fluxes are up to an order of magnitude larger in the eastern half of the Archipelago relative to those in the west. Much of the elevated mixing is concentrated near sills in Queens Channel and Barrow Strait, with stronger mixing particularly evident in the net shifts of the densest water to lower densities as it traverses these constrictions. Associated with these shifts are areally averaged buoyancy fluxes up to 10^{-8} m^2 s^{-3} through the 1027 kg m^{-3} isopycnal surface, which lies at approximately 100 m depth. This value is similar in strength to the destabilizing buoyancy flux at the ocean surface during winter. Effective diffusivities estimated from the buoyancy fluxes can exceed 10^{-4} m^2 s^{-1}, but are often closer to 10^{-5} m^2 s^{-1} across the Archipelago. Tidal forcing, known to modulate mixing in the Archipelago, is not included in the model. Nevertheless, mixing metrics derived from our simulation are of the same order of magnitude as the few comparable observations.

1. Introduction

The Canadian Arctic Archipelago is one of two conduits for outflow of cool, low-salinity water from the Arctic Ocean to the North Atlantic. Water in these channels (Figure 1) flows at a net rate of order 1 Sv [*Prinsenberg et al.*, 2009], with velocities within the channels predominately governed by four factors: sea level gradient, wind, tidal currents, and buoyant boundary currents. Both modeling and observational studies agree that seasonal and interannual variability of net volume transport though the Archipelago is driven by sea level differences between the Beaufort Sea and Baffin Bay [e.g., *Peterson et al.*, 2012; *McGeehan and Maslowski*, 2012; *Lu et al.*, 2014]. Sea levels in the Beaufort Sea are primarily controlled by the wind regime, while those in Baffin Bay are linked to air–sea heat exchanges in the Labrador Sea [*Houssais and Herbaut*, 2011]. Indeed, *Hu and Myers* [2014] predict a significant decrease to the flux through Parry Channel in the coming century due to lifting of the sea surface in Baffin Bay. On daily and weekly timescales, tidal currents are responsible for much of the velocity variance [*Prinsenberg and Bennett*, 1989]. In many places, root-mean-square currents exceed 0.1 m s^{-1} and peak velocities exceed 1 m s^{-1} [*Hannah et al.*, 2009]. These channels also have strong buoyant currents (0.1–0.4 m s^{-1}) that oppose the mean flow, narrowly confined to the northern and eastern sides of the channels by geostrophy. Currents far from the boundary (>15 km) are weak.

To date, most studies of the Archipelago have focused on the two main channels: Parry Channel, which runs approximately east–west and provides an exit for Pacific Water that passed through Bering Strait, and Nares Strait, which is perpendicular and contains a significant component of Atlantic Water [*Münchow et al.*, 2007]. The "Central Sills Area" north of Parry Channel has seen less study, likely a combination of its remoteness, short ice-free season, and smaller volume fluxes. Nevertheless, the complex topography and strong tidal currents in this area have implications for water ultimately leaving the Archipelago.

Several observations point to the Central Sills Area as a key location within the Archipelago with respect to mixing. Point measurements from the early 1980s show significant slopes in the isohalines in both directions toward Penny Strait, with isohalines from 70 to 80 m deep in northern Archipelago outcropping at the

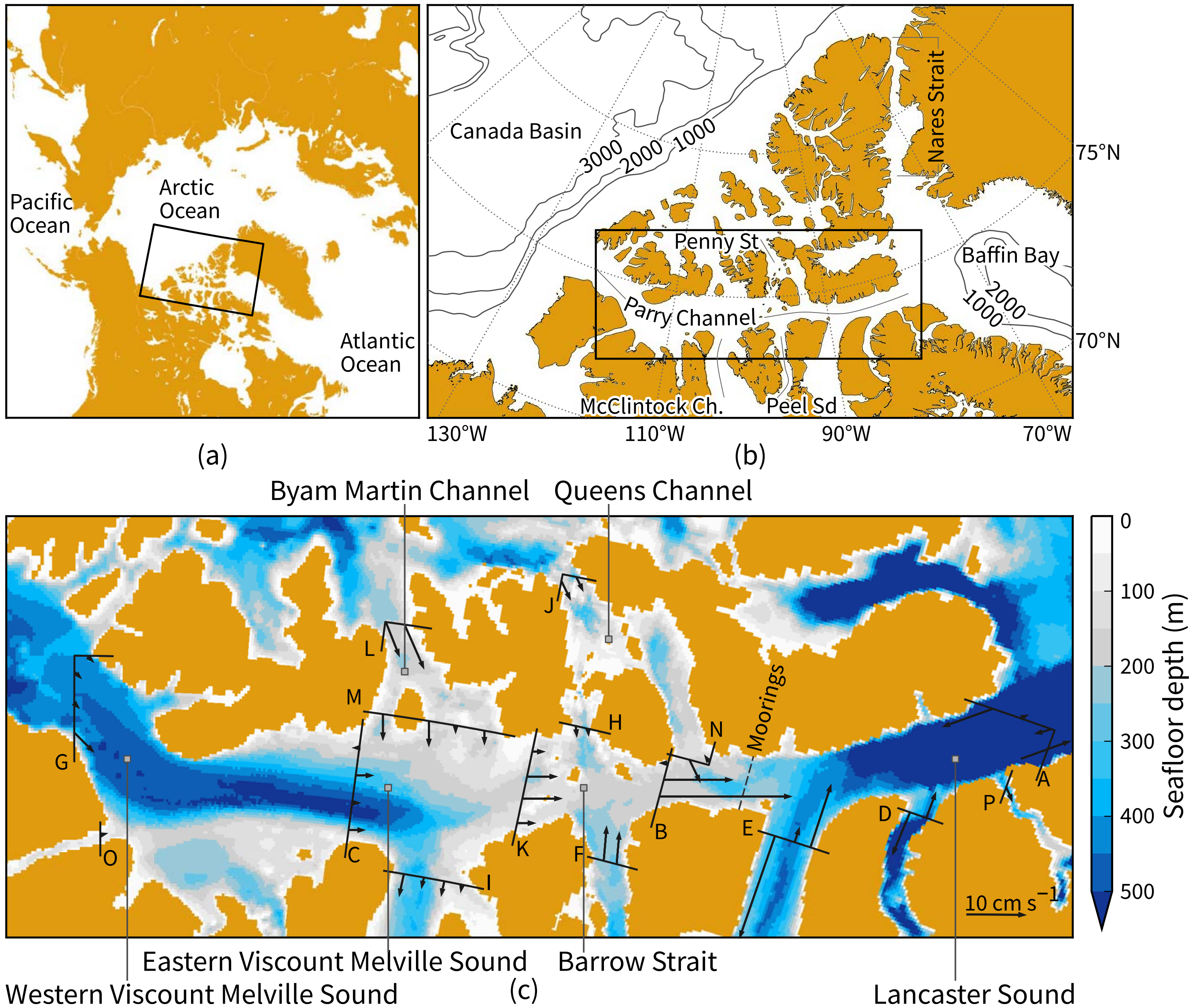

Figure 1. (a) Location of the Canadian Arctic Archipelago. (b) Enlargement of the region outlined in Figure 1a. (c) Coastline and bathymetry in the model configuration for the region outlined in Figure 1b. In this paper the Archipelago is divided into six named regions demarcated by the 16 labeled cross sections. Sections lie along the model grid, hence the need for corners in some sections, and arrows represent the net along-channel velocity. Here we denote the upper central part of Figure 1c as the "Central Sills Area."

surface [*de Lange Boom et al.*, 1987]. Similarly, during these studies in the 1980s and prior, Penny Strait and Queens Channel were consistently observed to have the highest surface salinity within the Archipelago. Based on the climatology of *Kliem and Greenberg* [2003], a maximum in surface density also occurs in this region (Figure 2). Another indicator of strong mixing is a local minimum in sea ice coverage. Additional heat bought to the surface by diapycnal mixing is manifest through visible and invisible polynyas [*Melling et al.*, 2015], which are ice-free or thin ice regions, respectively. Satellite images identify a number of sites in the Central Sills Area where polynyas consistently occur or ice breaks up comparatively early.

A number of physical processes cause elevated mixing within the Archipelago. These include wind, convection, shear instabilities, breaking large-amplitude internal waves, and boundary layers at the seafloor and ice–ocean interface. Both *Marsden et al.* [1994a] and *Crawford et al.* [1999] observed large, but short-lived, peaks in dissipation due to passing internal waves. *Marsden et al.* [1994b] attributed the observed near-surface internal waves to interaction of tidal flow with nearby ridged ice. These waves were necessary to create sufficient shear to induce mixing in the pycnocline. Below the pycnocline but away from the seafloor, active mixing events identified by enhanced dissipation rates have been observed over a range of depths

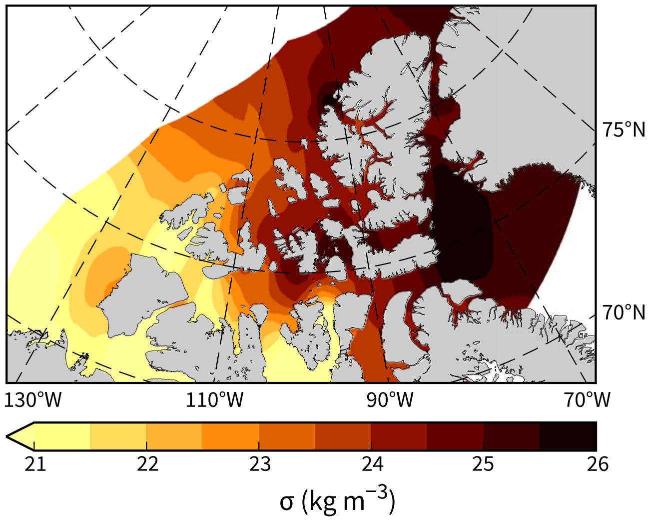

Figure 2. Surface density anomaly across the Archipelago. Contours are calculated using surface temperature and salinity from the climatology produced by *Kliem and Greenberg* [2003], which is centered around the time of minimum ice coverage. Note the denser water in the central channels.

[*Crawford et al.*, 1999]. These shear-induced events had vertical scales of 10–20 m. Near the seafloor in Barrow Strait, *Prinsenberg and Bennett* [1987] observed bottom mixed layers up to 50 m thick. All of these studies conclude that mixing is tidally modulated, with turbulence more energetic during spring tides. This is most apparent in the surface mixed layer and the pycnocline.

The complexity of the Archipelago limits the generalizability of these mixing studies to other locations or time periods. Consequently, there is a lack of quantitative mixing estimates with which spatial and/or seasonal variability can be discerned. Such estimates would complement the many existing studies concerned with freshwater and volume fluxes through the Archipelago. Identifying where water mass modification occurs allows for a more complete conceptual understanding of throughflow in the Archipelago. Additionally, it suggests where to focus effort for further targeted mixing studies.

In this paper, we use a 1/12° resolution model run for 2002–2010 (section 2). We analyze simulated volume fluxes, density structure, and sea ice conditions (section 3) insofar as necessary to explain mixing variability. Then, by using cross sections to demarcate six contiguous regions of the Archipelago, we estimate mixing strength across the Archipelago and how this changes with season and location (section 4). Our estimates focus on waters with potential densities equal to or greater than 1027 kg m^{-3}, which is the approximate mean density of Pacific Water in the Canada Basin. These waters typically lie below 100 m meaning that direct advective flux of their properties across the Archipelago is limited by sills such as those in Penny Strait (80 m) and Barrow Strait (125 m). They also seldom experience direct ventilation during winter convective mixing. Last, we consider the validity of our estimates, the implications for water mass modification, and the causes of mixing variability (sections 5 and 6).

2. Model Description

The model configuration used in this study, the Arctic and Northern Hemisphere Atlantic 1/12° (ANHA12), uses the Nucleus for European Modelling of the Ocean (NEMO) *[Madec and the NEMO team*, 2008] version 3.4 framework coupled with the Louvain-la-Neuve (LIM2) [*Fichefet and Morales Maqueda*, 1997] sea ice model with an elastic-viscous-plastic rheology. The ocean model is three-dimensional and hydrostatic with a free surface. In the vertical, 50 *z*-levels are used along with partial steps. Horizontally, the grid consists of 1632 $\times$ 2400 grid points and contains the whole Arctic Ocean (with Bering Strait at the boundary) and the Atlantic Ocean as far as 20°S. Within the Archipelago, the model has a resolution of $\sim$4 km. Typical channels contain 10–20 grid cells in the across-channel direction and 20–25 vertically. Consequently, the model has the ability to resolve, or at least permit, buoyant coastal currents within the channels. Such currents are ubiquitous in the Archipelago and constitute much of the component of flow toward the Arctic.

Vertical mixing of tracers within the model is treated using a turbulent kinetic energy (TKE) closure scheme. The diffusivity coefficients are computed based on a prognostic equation for TKE and an assumption about the turbulent length scales. The prognostic equation includes production by vertical shear, and reduction by stratification, vertical diffusion, and dissipation (see *Madec and the NEMO team* [2008]). A minimum vertical diffusivity of 10^{-6} m^2 s^{-1} is applied to avoid numerical instabilities associated with weak vertical diffusion. Conversely, where the water column is unstable or neutrally stable (buoyancy frequency of less than 10^{-6} s^{-1}), the vertical diffusivity is set to 10^{1} m^2 s^{-1}.

Lateral mixing in the model is calculated along isoneutral surfaces, reducing horizontal diffusion across tilted isopycnals. The harmonic diffusivity is grid-size-dependent with a maximum of 50 m^2 s^{-1}, but is approximately 20 m^2 s^{-1} within the Archipelago. We expect overly diffusive downslope flows as no bottom boundary layer scheme was included [e.g., *Beckmann and Döscher*, 1997]. Note that these mixing parameters were chosen before this paper was proposed.

ANHA12 was run for 2002–2010 with initial and boundary conditions given by the global ocean reanalysis and simulation (GLORYS1v1) [*Ferry et al.*, 2010] and an early version of the Canadian Meteorological Centre's global deterministic prediction system reforecasts (CGRF) atmospheric forcing, including uncorrected precipitation fields [*Smith et al.*, 2013]. No tidal forcing is included. Five day means of a range of quantities for each grid cell are saved, and our analysis focuses on density and velocity in six regions demarcated by sixteen cross sections within the Archipelago. The names used to refer to these six regions throughout the text are given in Figure 1c.

3. Simulated Hydrography

3.1. Flow Structure and Fluxes

Qualitatively, ANHA12 simulates the expected average flow structure within the Archipelago: strong coastal flows superimposed on a generally southward and/or eastward flow. This is evident in the along-channel velocities at each cross section averaged over the entire simulation period (Figure 3). With the fluxes displayed in this manner, it is clear that much of the toward-Atlantic flow (red) is composed of barotropic coastal flows on the south or west sides of channels. Conversely, the toward-Arctic flow (blue) is much weaker and often away from the surface. Such flow structure is observed in mooring data from western Lancaster Sound [*Prinsenberg et al.*, 2009, see Figure 1c for mooring location]. Indeed, *Peterson et al.* [2012] note that flow through this region is adequately monitored by measuring flux through only the southern half of the channel.

Section F (Peel Sound) is noteworthy as it has a net northward flow. This results from the sill in western Barrow Strait (97°W) steering flow southward through McClintock Channel, with this flow then returning northward to join the eastward flow through Parry Channel [e.g., *Wang et al.*, 2012].

Within the channels, a simple measure of the relative importance of barotropic and baroclinic forcing is to consider the positive and negative components of the net flux. Figure 4 shows volume flux partitioned by sign of along-channel velocity for water entering and exiting the entire Parry Channel (Figures 4a and 4b), the center of Parry Channel (Figures 4c and 4d), and the Central Sills Area (Figures 4e and 4f). Of these sites, those in the center of the Archipelago show minimal exchange flow for most times of the year (Figures 4c–4f). Typically the toward-Arctic component is an order of magnitude smaller than the net flux at these central sites. Nevertheless, there is a clear negative correlation between the flux components: the toward-Arctic flux is maximum when the toward-Atlantic flow is minimum. This suggests that the toward-Arctic flow is masked by the stronger overall toward-Atlantic flow. A stronger exchange flow can therefore be expected in years with a smaller overall sea level difference.

The timing of the peak in toward-Arctic flux, which occurs in early autumn, agrees well with the aforementioned mooring data. There is also some agreement between these data and the simulated net flux at the location of the moorings (Figure 4g). The agreement is better for the first 3 years of simulation. Thereafter the simulated fluxes are noticeably larger. This is related in part to issues with the interpolation of runoff onto the model grid, which has been fixed for future experiments. Overestimates of a similar magnitude are also simulated by *Wekerle et al.* [2013] and *Lu et al.* [2014]. Note also that our simulation suggests large fluxes in the early months of the year, whereas observations suggest a minimum at this time. An early peak flux is also simulated by *McGeehan and Maslowski* [2012] who discuss several reasons for the discrepancy, in particular that flow in the northern half of the channel is given too little weight in estimates of net flux from moorings. Indeed, in mid-2006, the two northernmost of the four moorings in Barrow Strait were removed [*Peterson et al.*, 2012]. There is a noticeable difference in the mean net flux observed before and after this time.

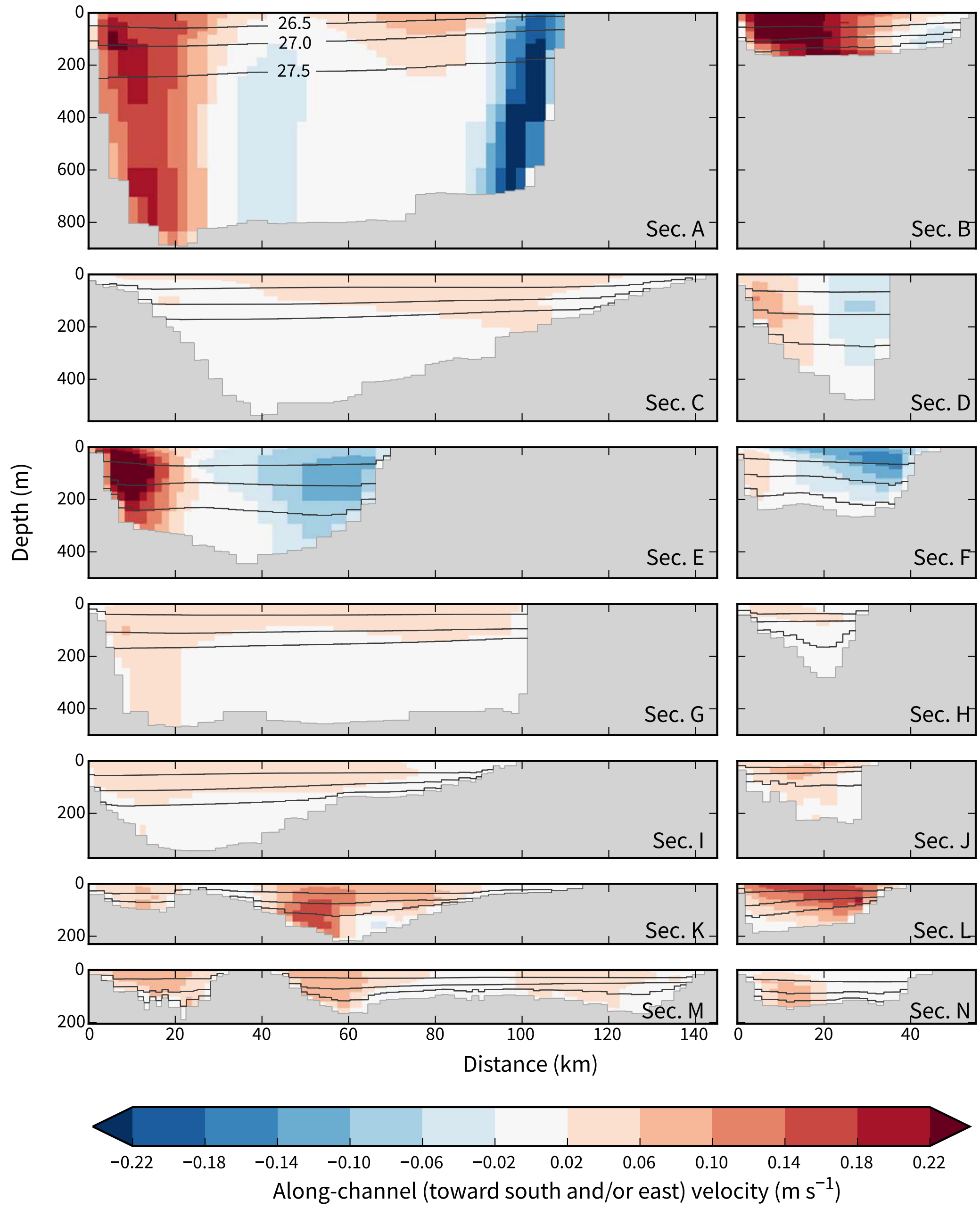

Figure 3. Simulated cross-sectional flow structure. Velocities are the mean over the whole simulation period (2002–2010) and density contours are the mean depths of the σ_θ=26.5, 27.0, and 27.5 kg m^{-3} isopycnals. In all plots, the southern or western coast is on the left hand side. See Figure 1c for section labels and note that for sections with a corner, we present velocities interpolated along a straight line between the ends of the section. Sections O and P, each only five grid cells wide, are not shown.

Flux through eastern Lancaster Sound (section A, Figure 4b) is noticeably different from the other sections in that the toward-Arctic component is stronger than the net flow. This flow results from a strong coastal current from Baffin Bay that recirculates in the mouth of the Sound [e.g., *Prinsenberg et al*., 2009; *Wang et al*., 2012]. The coherent inflow and outflow regions dominate the velocities for this section (Figure 3a). Remnants of the inflow can be identified in Wellington Channel (Figure 3n); [see also *de Lange Boom et al*., 1987], but the current significantly weakens during its 300–400 km transit along the northern side of Lancaster Sound.

The seasonal cycles of net flux through each of the sections correlate strongly with each other, with the highest fluxes at or just after the new year and the lowest fluxes late in the year. To some extent, this

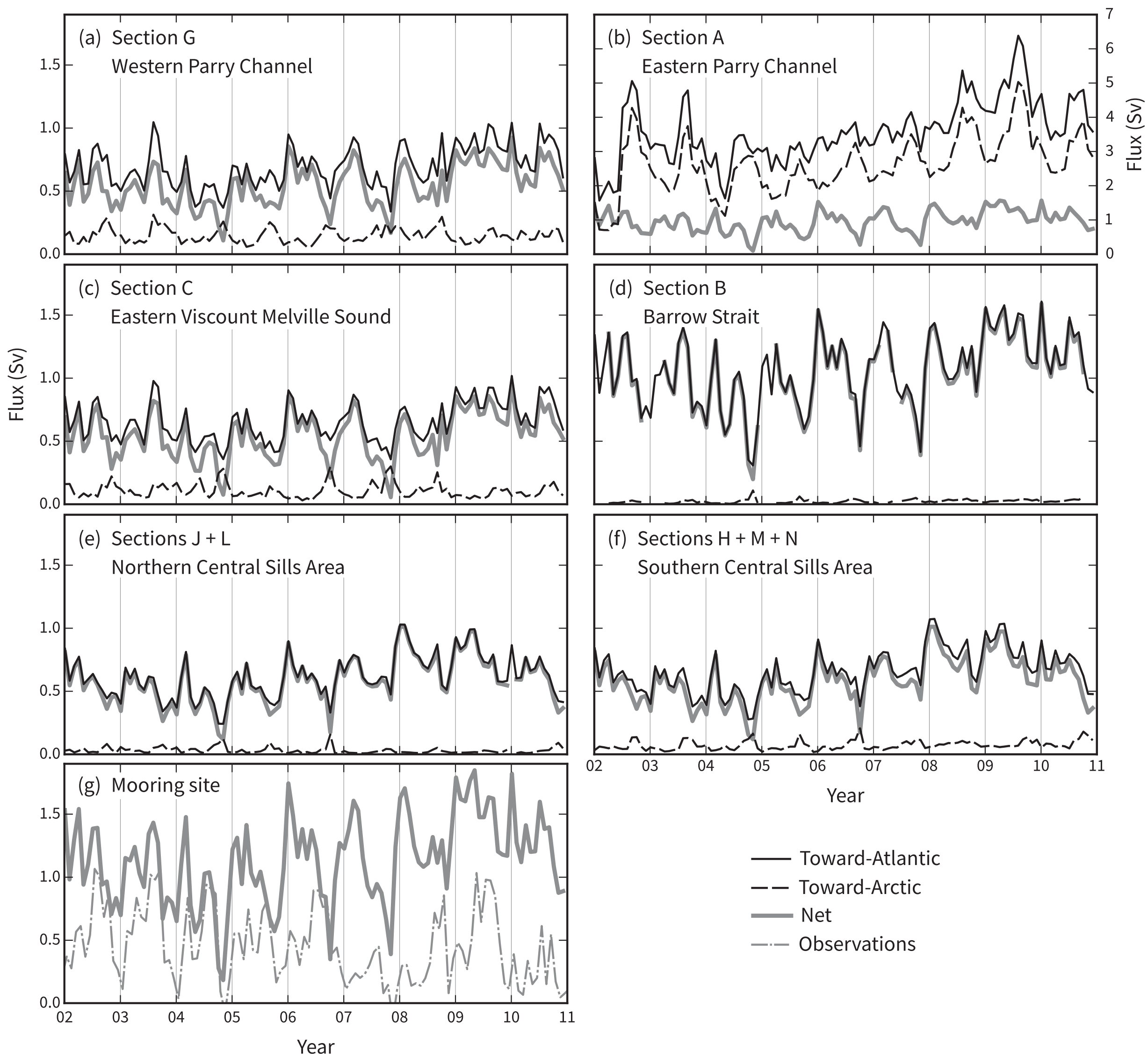

Figure 4. (a–f) Simulated fluxes at various sections throughout the Archipelago partitioned by along-channel velocity. Note that a different *y*-axis is used for section A. (g) Simulated fluxes at the mooring transect (Figure 1c) compared against observations [*Peterson et al.*, 2012].

correlation is expected as sections are not independent. Nevertheless, that the north–south and east–west fluxes correlate strongly agrees with previous studies that note that flow through individual channels is primarily driven by the same large-scale atmospheric forcing [*Houssais and Herbaut*, 2011; *Wekerle et al.*, 2013].

3.2. Density Structure

The density structure across the Archipelago (Figure 5) highlights the importance of processes that transport properties vertically, especially for water at depth. The center of the Archipelago is shallower than the areas to the west, north, and east. Consequently, distinct differences exist in the density structure at depth depending on location within the Archipelago. In both Parry Channel and the northern Archipelago, isopycnals of 27 kg m^{-3} or more occur noticeably higher in the water column on the western or northern sides of the transect. Buoyancy fluxes up through these isopycnals influence how strongly water properties are communicated across the Archipelago.

North of the shallow sills in Queens Channel, isopycnals slope upward toward the south. This is consistent with the isohalines shown by *Fissel et al.* [1984, their Figure 21] along a very similar transect taken in March–April 1983. Similarly, isohalines from their transect through Parry Channel (their Figure 18) are consistent

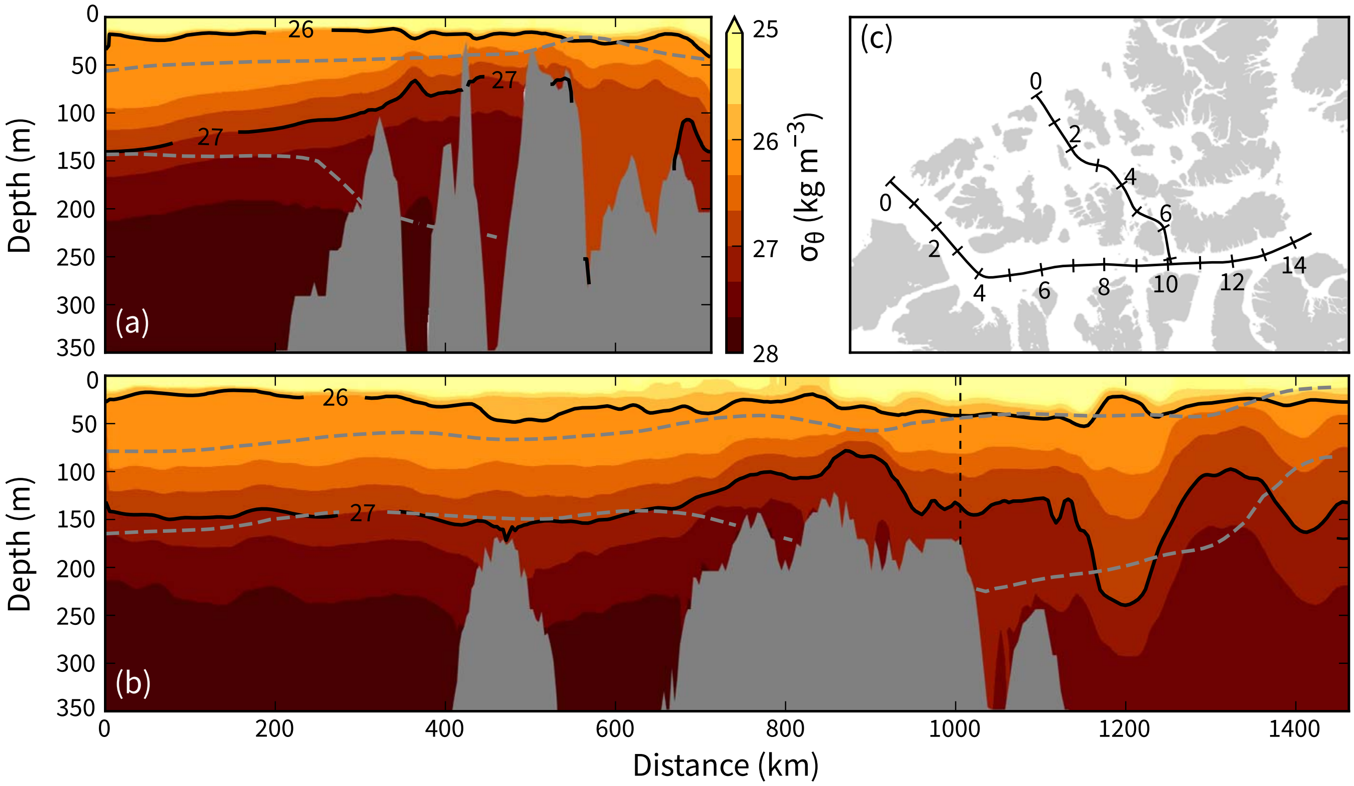

Figure 5. The potential density field in early September 2003 through (a) the northern Archipelago and (b) Parry Channel. Dashed, grey contours show the 26 and 27 kg m^{-3} isopycnals calculated from the climatology produced by *Kliem and Greenberg* [2003]. (c) Distances in multiples of 100 km. The final 35 km of the northern transect lie within Parry Channel and the vertical dashed line indicates the intersection of the two transects.

with the simulated field shown in Figure 5b. These authors attribute the reduced salinity, and hence density, in the east to the influence of Baffin Bay Atlantic Water in place of Canada Basin Atlantic Water. Note that below approximately 200 m, water in Baffin Bay is fresher than in the Canada Basin and vice versa above.

A comparison between the modeled density field and a climatology centered on September 1 is given for two isopycnals in Figure 5. This climatology is calculated from sparse data, especially in the northwest (see Figure 3 of *Kliem and Greenberg* [2003]), and does not account for sills separating water masses. Consequently, it cannot capture the upward tilt in 27 kg m^{-3} isopycnal at 0–500 km in Figure 5a. The depth of this contour at each end of the transect, however, is reasonable. Similarly, the depths of climatological and modeled isopycnals broadly agree throughout Parry Channel (Figure 5b). Note that although fields shown in Figure 5 represent data at only one time, the picture remains similar throughout the simulation. Typical interannual variation of the depth of a given isopycnal is 10–20 m.

3.3. Sea Ice Conditions

A thorough description of sea ice conditions is in preparation [*Hu et al*., Simulated sea ice growth in the Canadian Arctic Archipelago region] but outside the scope of this study as it will have at most a minor influence here given our focus on deeper waters. Consequently, we review only briefly the simulated conditions. We also note that despite suggestions of enhanced mixing through ice–current interactions (section 1), sea ice typically acts to inhibit mixing by reducing momentum transfer from the atmosphere [e.g., *Rainville et al*., 2011].

For 8–10 months of the year, sea ice coverage is 80–100% throughout the Archipelago. The thickest ice (4–5 m) occurs at the northern and western boundaries. Here ice thickens dynamically as it approaches the many islands. The thinnest ice (0–2 m) occurs at the outlets to Baffin Bay, where the ice undergoes large seasonal variations. Simulated ice thickness within the Archipelago and over the continental shelf to the northwest agrees well with IceBridge (airborne laser altimetry), ICESat (satellite lidar), and drilled thickness observations [*Lindsay*, 2013].

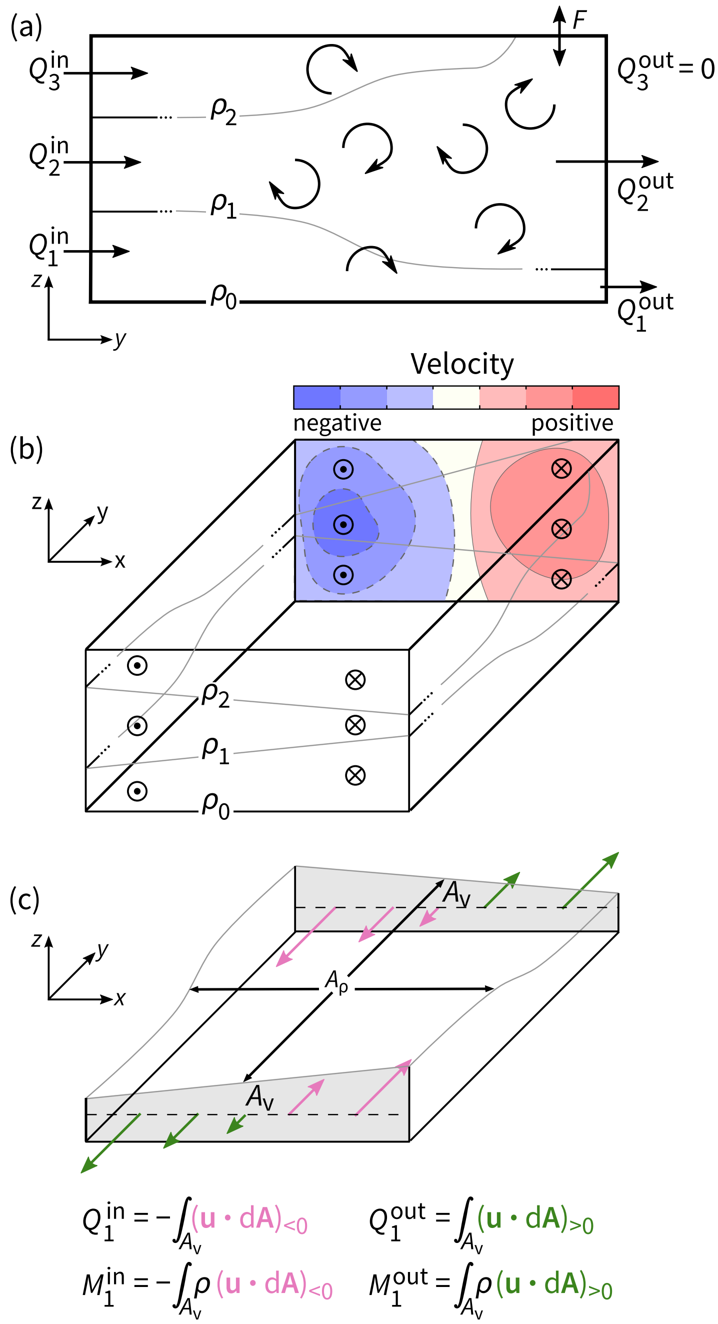

Figure 6. Concept, notation, and scheme used to estimate diapycnal diffusivity. (a) In unidirectional flow within a channel, diapycnal mixing causes isopycnals to slope and causes changes to mass transport as a function of density. (b) Extending the concept from Figure 6a to a three-dimensional, rectangular channel and allowing for lateral differences in flow direction. (c) Definition of the volume Q_1 and mass M_1 fluxes for the densest layer. Subscript '>0' implies only positive values are included in the integration and vice versa, and minus signs for the inward fluxes ensure all fluxes are nonnegative.

4. Mixing Rates Throughout the Archipelago

Prior knowledge of the hydrography throughout the Archipelago (section 1) suggests there is variation across the Archipelago with respect to mixing levels, with the strongest mixing expected in the Central Sills Area. By quantifying mixing in different regions of the Archipelago, we will estimate the magnitude of this variation. In doing so, we also ascertain the fate of water transiting the Archipelago. For example, dense water may flow through the channels unchanged or may completely mix with the water above.

4.1. Inverse Estimates of Diapycnal Diffusivity and Buoyancy Flux

Analysis of changes in transport as a function of density between the incoming and outgoing flows in a channel allows estimates of diapycnal diffusivities and buoyancy fluxes. Here we estimate these quantities (i) spatially averaged over the region enclosed by cross sections and (ii) temporally averaged over monthly timescales.

Conceptually, the method is encapsulated in Figure 6a. Assume a well-stratified flow enters the left end of the channel and that total transport is spread somewhat evenly amongst all densities ($Q_1^{in} \approx Q_2^{in} \approx Q_3^{in}$). Mixing within the channel causes the least and most dense layers to mix with the middle density layers. Consequently, transport out of the channel is dominated by middle density water ($Q_2^{out} > Q_1^{out}, Q_3^{out}$). For flow within the Archipelago, this concept needs to be extended to three-dimensional flow to allow for lateral variation in flow direction (Figure 6b). Specifically, the inward and outward fluxes no longer correspond with one end of the channel each (Figure 6c). Not demonstrated in Figure 6 is the potential for the total mass within the channel to change due to a flux of, say, denser water that is then stored within the channel rather than being mixed upward.

Mathematically, the method uses the advection–diffusion equation for mass within a variable volume V:

$$\frac{\mathrm{d}}{\mathrm{d}t}\int_V \rho_\theta \,\mathrm{d}V + \int_V \nabla\cdot(\rho_\theta \mathbf{u})\mathrm{d}V + F = \int_V \nabla\cdot(K\nabla\rho_\theta)\,\mathrm{d}V \tag{1}$$

where ρ_θ is potential density, $\mathbf{u}$ is velocity, and K is the diffusivity of density. Any surface buoyancy exchange due to ice growth and melt and atmospheric and solar forcing is included in F. This term is nonzero when part or all of the upper surface of V coincides with the sea surface; see, for example, the ρ_2 isopycnal in Figure 6a. Positive values for F correspond to a stabilizing flux (warming or freshening).

Applying the divergence theorem, equation (1) becomes

$$\frac{\mathrm{d}}{\mathrm{d}t}\int_V \rho_\theta \,\mathrm{d}V + \oint_A \rho_\theta \mathbf{u}\cdot \mathrm{d}\mathbf{A} + F = \oint_A K\nabla\rho_\theta \cdot \mathrm{d}\mathbf{A} \tag{2a}$$

$$\approx \int_{A_\rho} K\frac{\partial \rho_\theta}{\partial z}\,\mathrm{d}A_h \tag{2b}$$

$$\approx \bar{K}\int_{A_\rho} \frac{\partial \rho_\theta}{\partial z}\mathrm{d}A_h \tag{2c}$$

where A is the total area enclosing V, A_ρ is the isopycnal surface at the top of the integration volume, and A_h is the projection of A_ρ onto the horizontal plane. The right-hand side is first simplified by noting that the total area through which diffusion occurs is dominated by A_ρ. Further, we rely on the large aspect ratio of the volume V to use the vertical density gradient in place of its diapycnal counterpart. The second step defines an effective mean turbulent diffusivity $\bar{K}$ through the isopycnal surface. Note that the expression in equation (2b), which is the residual of the three terms on the left hand side, is closely related to the integrated buoyancy flux across the isopycnal surface:

$$\int_{A_\rho} J_\mathrm{b}\,\mathrm{d}A_h = \frac{-g}{\rho}\int_{A_\rho} K\frac{\partial \rho_\theta}{\partial z}\,\mathrm{d}A_h = \int_{A_\rho} KN^2\mathrm{d}A_h \tag{3}$$

where J_b is buoyancy flux in units of $\mathrm{m^2\,s^{-3}}$ (or equivalently $\mathrm{W\,kg^{-1}}$) and N is the buoyancy frequency.

The continuity equation provides a link between three quantities, two of which are derived directly from the model: the net flux through the vertical sides of the volume and the rate of change of the volume V beneath the isopycnal surface. The difference between these gives the advective flux through the isopycnal surface:

$$\int_{A_\rho} \mathbf{u}\cdot \mathrm{d}\mathbf{A} = -\int_{A_v} \mathbf{u}\cdot \mathrm{d}\mathbf{A} - \frac{\mathrm{d}V}{\mathrm{d}t} = (Q_1^\mathrm{in} - Q_1^\mathrm{out}) - \frac{\mathrm{d}V}{\mathrm{d}t} \tag{4}$$

Q_1^in and Q_1^out are defined in Figure 6c.

To summarize our method and make the result more intuitive, we rewrite equation ((2a)c) and invoke the notation shown in Figure 6c:

$$\underbrace{-(M_1^\mathrm{in}-M_1^\mathrm{out}) + \rho_1(Q_1^\mathrm{in}-Q_1^\mathrm{out})}_{\text{horizontal mass divergence}} + \underbrace{\frac{\mathrm{d}}{\mathrm{d}t}\int_{V_1}\rho_\theta \mathrm{d}V - \rho_1\frac{\mathrm{d}V_1}{\mathrm{d}t}}_{\text{mass rate of change}} + F = \underbrace{\bar{K}_1\int_{A_1}\frac{\partial\rho_\theta}{\partial z}\mathrm{d}A_h}_{\text{diffusive buoyancy flux}} \tag{5}$$

The effective diffusivity on any isopycnal is found by selecting a desired isopycnal ρ_1, undertaking the areal and volume integrals, and then solving for $\bar{K}_1$. Note that the various terms are collected such that each of the three braced expressions have comparable magnitude.

The quantities used in equation (5) are all calculated using 5 day means: vertical density gradients are evaluated on grid cell faces using finite differences of adjacent density values and the associated depths at the cell centers; rates of change, which stem predominantly from seasonal changes in water masses, are estimated using a central finite difference; and the surface buoyancy exchange F is derived from several mean surface quantities such as heat flux and ice growth rate. By using 5 day means, uncertainty is introduced to the left-hand side of equation (5) in two ways. First, advective mass flux and surface buoyancy flux are approximated as the products of means, not the means of products. Second, rates of change will be smoothed estimates of their true values. We reduce the influence of these uncertainties by considering changes on monthly timescales.

4.2. Flux Versus Density

Expressing flux as a function of potential density can demonstrate whether there is strong mixing within a particular region. To do this, we calculate inward and outward fluxes as in Figures 6a and 6c, with density bins of 0.1 kg m^{-3}. The inward fluxes are shown in Figure 7 together with the net change (outward – inward). Fluxes were averaged across 1 year of data to minimize the effect of seasonal density changes. Results are shown for only 2005, but the other years are qualitatively similar.

For all regions except Lancaster Sound, the average flux into the region is dominated by water with a potential density anomaly of approximately 26.5 kg m^{-3}. There is also a significant contribution to the inward flux by dense water (27.5–28.0 kg m^{-3}) in the two deepest regions, western Viscount Melville Sound and Lancaster Sound.

Barrow Strait and Queens Channel display a distinct loss of the denser water flowing into the channel, with a corresponding increase in water of slightly lower density. This change is consistent with strong mixing within the channel as shown conceptually in Figure 6a. Similar net changes are not as evident in the other four regions, at least relative to the inward flux. This suggests Queens Channel and Barrow Strait will have the strongest mixing rates, but to substantiate this statement we need to evaluate the diffusivity and buoyancy flux.

4.3. Regionally Averaged Mixing

Time series of effective diffusivity in each region are evaluated on 10 isopycnals (σ_θ=26.8, 26.9, ..., 27.7 kg m^{-3}). This range is chosen for three reasons. First, it corresponds to water whose direct advective flux is at least somewhat limited by sills as described in section 3.2. Second, it broadly corresponds to the density range of Pacific Water in the Canada Basin of the Arctic Ocean [*Carmack et al.*, 2008, 2016]. Third, it avoids volumes that are strongly influenced by buoyancy flux at the ocean surface. Shallower isopycnals are addressed in section 4.4.

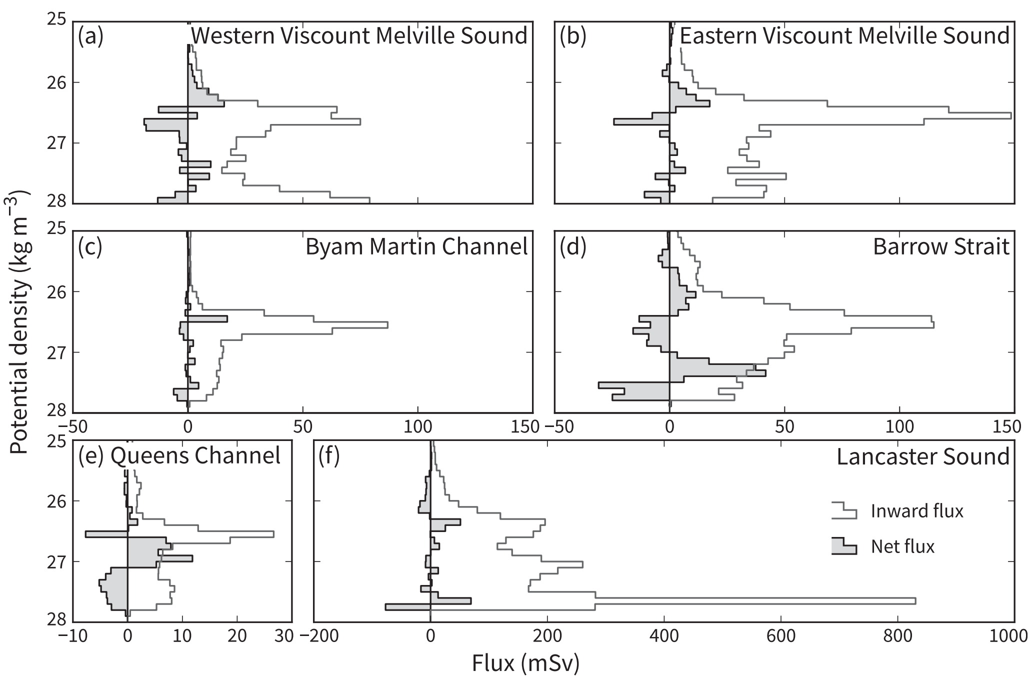

Figure 7. Changes in the composition of volume flux between water flowing into and out of the six regions. Fluxes are an average across a year (2005), potential density bins are 0.1 kg m^{-3}, and a positive net flux for a given density bin signifies that outflow is greater than inflow. Inward fluxes, as defined in Figure 6c, are the summed flux for all water with a velocity into the region through any of the bounding cross sections. Note that no water exceeded $\sigma_\theta = 28$ kg m^{-3} and flux for water with $\sigma_\theta < 25$ kg m^{-3} is insignificant.

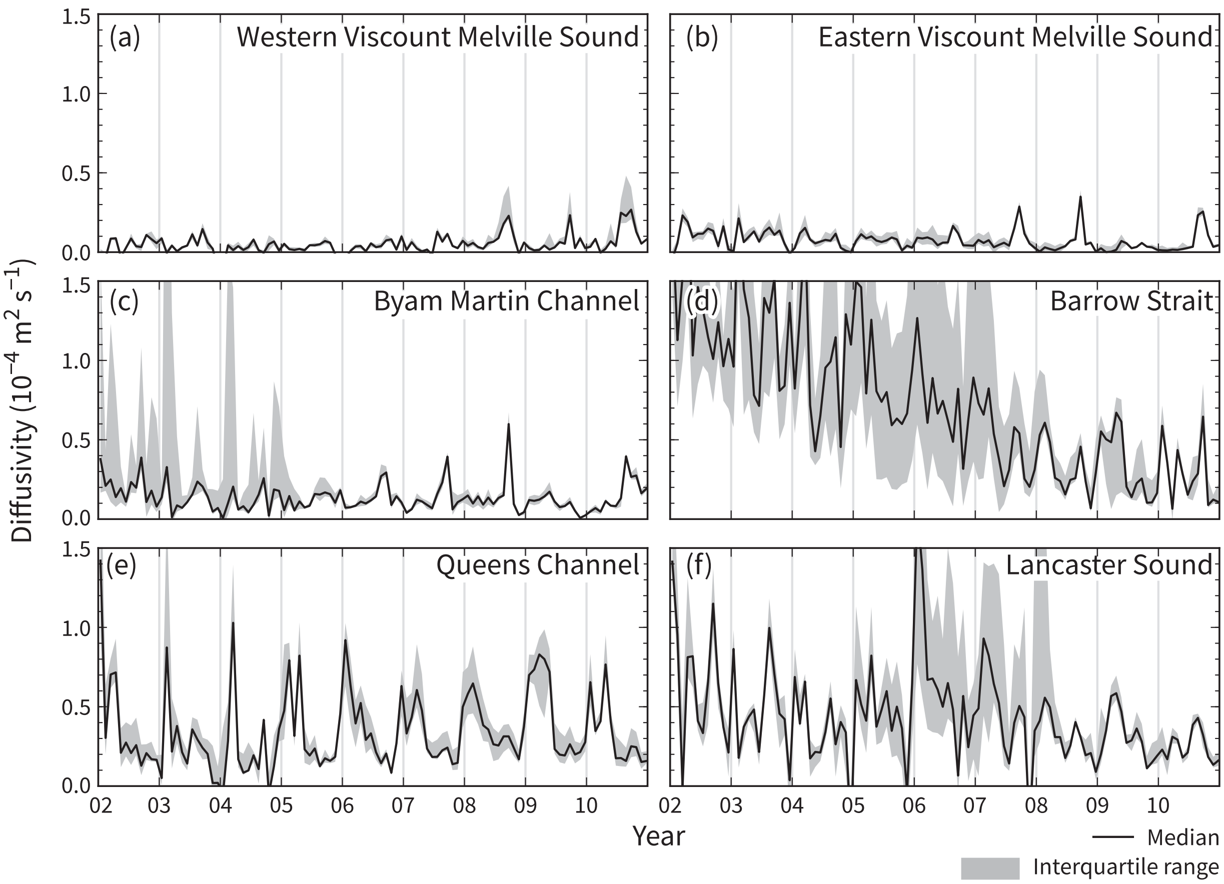

Figure 8. Regionally averaged diffusivity ($\bar{K}$) exhibiting strong spatial and seasonal variability. Monthly averages were evaluated on 10 isopycnal surfaces (σ_θ=26.8, 26.9, . . . , 27.7 kg m^{-3}), with the median and quartiles calculated from these 10 values.

Two results are evident in the time series (Figure 8). First, a seasonal cycle is evident in each series. There is also some evidence for interannual variability, but we do not investigate this here given the short simulation length. Second, most diffusivities fall in the range $10^{-5}-10^{-4}$ m^2 s^{-1}. For comparison, values of this magnitude have been observed in Florida Strait and the New England Shelf, smaller values (10^{-6} m^2 s^{-1}) in much of the water column in the Black Sea Shelf north of the Bosphorus Strait [*Gregg et al.*, 1999], slightly larger values ($10^{-4}-10^{-3}$ m^2 s^{-1}) in Vema Channel in the Brazil Basin [*Hogg et al.*, 1982] and on the shelf near Monterey Canyon, California [*Gregg et al.*, 1999], and much larger values ($10^{-3}-10^{-1}$ m^2 s^{-1}) in other regions of complex topography such as the Romanche Fracture Zone in the mid-Atlantic Ridge [*Ferron et al.*, 1998] or Cordova Channel, British Columbia [*Lu et al.*, 2000]. Values in the open ocean at middepth are typically $10^{-6}-10^{-4}$ m^2 s^{-1} [*Whalen et al.*, 2012].

To understand the diffusivities derived, and more generally the fate of the water passing through different channels, we consider the cycles of each of the four terms in equation (5). These terms are shown in Figure 9 as volume fluxes for the regions with the smallest and largest diffusivities. In western Viscount Melville Sound, the budget is a near balance between the integrated rate of change of mass and the horizontal mass divergence. For example, if a given mass of dense water is advected into this region, it will tend to move through or be stored within the region with its properties unchanged as opposed to mixing with the water above it. Conversely, in Barrow Strait the horizontal mass divergence is noticeably larger than the density rate of change term. This is akin to the situation shown in Figure 6a in which differences in properties between the ends of a channel are significantly affected by mixing.

It is difficult to discern the nature of the seasonal cycle of diffusivities as they are currently presented (Figure 8). Therefore, Figure 10a displays the median diffusivity on the σ_θ=27.0 kg m^{-3} contour for each month of the year for each region. Each monthly median is calculated from nine values (one for each year of

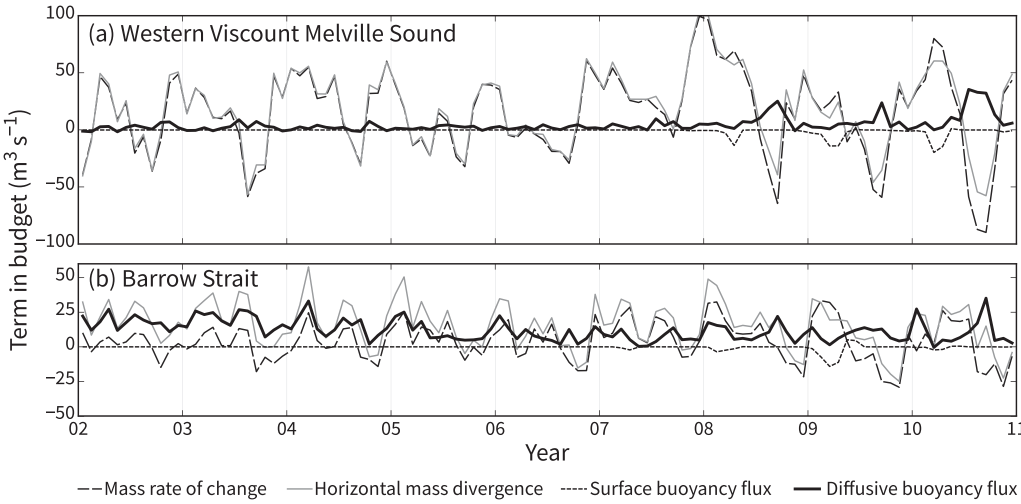

Figure 9. The terms in the water mass budget (equation (5)) for the regions with the smallest and largest diffusivities. The budgets shown are calculated for water beneath the σ_θ=27.0 kg m^{-3} isopycnal.

simulation). The three western regions exhibit one peak during the year. This peak occurs around late-summer. This time of year corresponds to both the minimum ice coverage and the maximum toward-Arctic fluxes (Figure 4). In contrast, the three eastern regions exhibit two peaks. In these regions the late-summer peak is minor in comparison to one around the new-year. This second peak occurs when the strongest volume fluxes typically occur.

To some degree, the diffusivities we have derived are influenced by stratification. Increased stratification limits diffusivity and vice versa. Therefore, we briefly consider alternative metrics that quantify mixing. These are the buoyancy flux J_b defined within equation (3) and turbulent dissipation rate ε given by

$$\varepsilon = J_b/\Gamma \approx 5J_b \quad (6)$$

where Γ is the mixing efficiency set as 0.2 [*Osborn*, 1980]. Plots of buoyancy flux (Figure 10b) look similar to those for effective diffusivity because stratification varies less than diffusivity. Using $\varepsilon \approx 5J_b$ suggests average turbulent dissipation rates of 3–5$\times10^{-8}$ m^2 s^{-3} in Queens Channel and Barrow Strait. For comparison, background dissipation rates of less than 10^{-8} m^2 s^{-3} have been observed in locations such as the New England Shelf [*Gregg et al.*, 1999] and rates of $10^{-8}-10^{-6}$ m^2 s^{-3} in Admiralty Inlet in Washington [*Seim and Gregg*, 1994] and over the Romanche Fracture Zone [*Ferron et al.*, 1998]. Values of 10^{-5}–10^{-3} m^2 s^{-3} can occur in the immediate vicinity of sills [e.g., *Klymak and Gregg*, 2004; *Staalstrøm et al.*, 2015]. These very high values reduce to $O(10^{-6})$ m^2 s^{-3} if they are averaged over an area of $O(1)$ km^2. Note that these comparisons are tenuous for two reasons. First, dissipation rate estimates can vary by orders of magnitude over a short time, short distance, or within a single profile. Second, there is some uncertainty in the value of the mixing efficiency and indications that it is not constant [*Ivey et al.*, 2008].

Interpreting the results in terms of total (areally integrated) buoyancy flux (Figure 10c) emphasizes the roles of the deeper regions, and vice versa, but does not change our conclusion of stronger mixing in the eastern Archipelago. Within the deeper regions, Viscount Melville Sound and Lancaster Sound, the 27.0 kg m^{-3} isopycnal surface has a large area. Conversely, for example, the 580–680 km region of Queens Channel in Figure 5a is insufficiently deep to host any water denser than 27.0 kg m^{-3}. Indeed, for part of the seasonal cycle, the total buoyancy flux in Queens Channel reduces to that of western Viscount Melville Sound. We note, however, that these values are significantly affected in part by how we designated the six regions in Figure 1c; for example, the ocean surface area of the western Viscount Melville Sound region is four times that of Queens Channel.

4.4. Surface and Near-surface Water Mass Modification

For 8 months of the year, the cold atmosphere either directly cools the near-surface water or induces ice growth and consequent brine rejection. These cause a destabilizing flux at the ocean surface (Figure 10d),

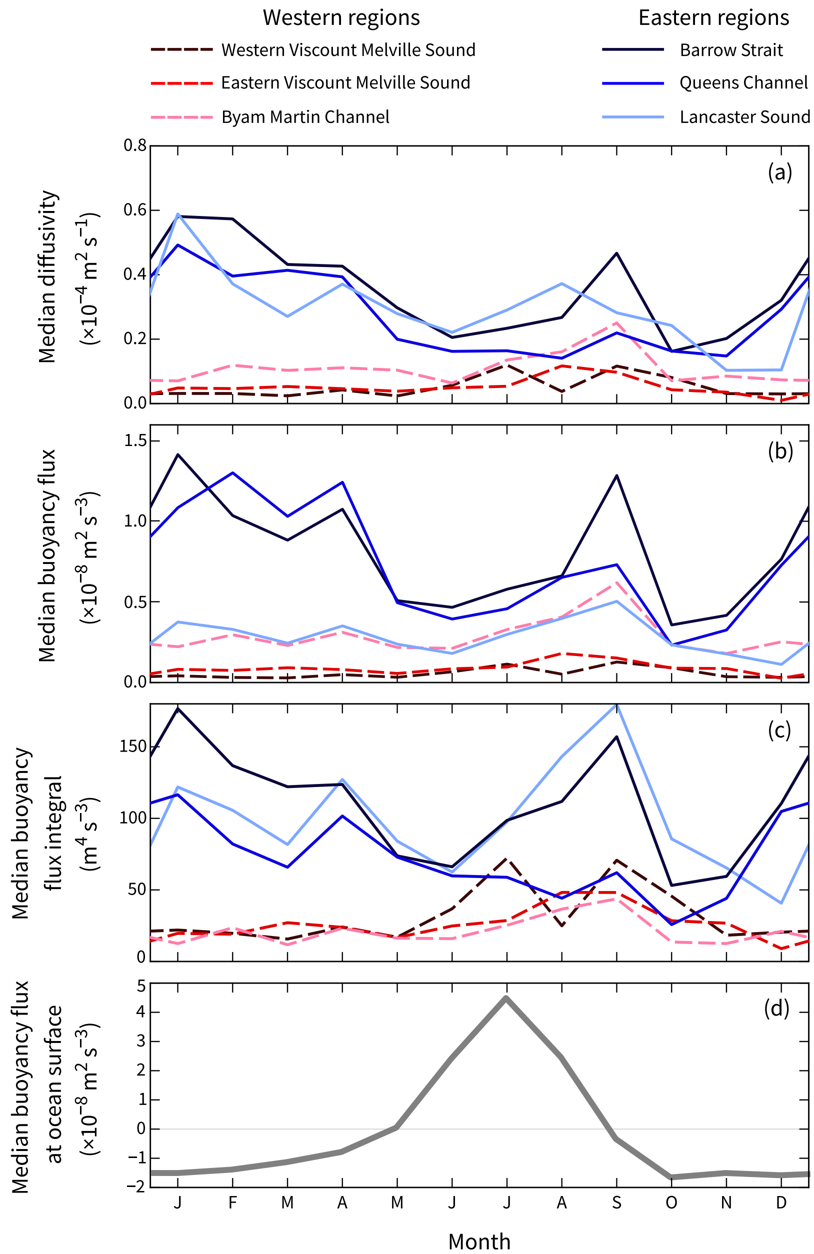

Figure 10. (a–c) Metrics of regionally averaged mixing evaluated on the $\sigma_\theta = 27.0$ kg m^{-3} isopycnal surface. Medians for each month were calculated from the values for 9 years of simulation. (d) Median buoyancy exchange at the ocean surface over all six regions.

which drives mixing of near-surface water. For the other 4 months, insolation and ice melt act to restratify the near-surface. The magnitude of the destabilizing flux reaches 1.5 $\times 10^{-8}$ m^2 s^{-3}. This is comparable to the buoyancy fluxes through the 27.0 kg m^{-3} isopycnals in Queens Channel and Barrow Strait for parts of the year. For the western regions, however, the ocean surface buoyancy flux is an order of magnitude larger than the diapycnal flux. In effect, variability in near-surface water mass properties is dominated by the buoyancy exchange with the atmosphere. Note that surface buoyancy flux is largely independent of location within the Archipelago.

To determine mixing rates in the near-surface water, we attempted the analysis from the previous section but for shallower isopycnals such as 26.0 or 26.5 kg m^{-3}. However, meaningful estimates of the diapycnal fluxes through these isopycnals is typically not possible. The buoyancy exchange F at the ocean surface is no longer a small term, so the diapycnal buoyancy flux is now the residual of three large terms (see equation (2a)). The uncertainty in each of the three terms (see section 4.1) results in an uncertainty in the residual comparable to its magnitude.

There were short periods that allowed a reasonable estimate of the diapycnal flux through the 26.5 kg m^{-3} isopycnal, which is typically half as deep as the 27.0 kg m^{-3} isopycnal (Figure 3). These periods occurred early in the simulation, when stronger ice cover mediated surface exchange. During this time, the buoyancy fluxes through the shallower isopycnal displayed similar magnitudes to those described in the previous section.

5. Discussion

5.1. Predicting Mixing Without Tides

The ANHA12 model used in this study does not contain tides, a trait shared by most other existing models of the Archipelago at similar resolutions [*Houssais and Herbaut*, 2011; *Wang et al*., 2012; *Wekerle et al*., 2013; *Lu et al*., 2014]. It is therefore arguably a poor choice for a study concerned with estimating mixing rates in a region in which mixing is strongly linked to tidal flow [*Hannah et al*., 2009; *Melling et al*., 2015] and contains sills that are substantially longer than a tidal excursion. Indeed, a range of quantities related to mixing have been observed or simulated to vary fortnightly with the spring–neap cycle: turbulent energy, velocity shear, eddy diffusivity, nutrient flux, and tidal dissipation [*Prinsenberg and Bennett*, 1987; *Marsden et al*., 1994b; *Hannah et al*., 2009].

Tides within the Archipelago can generate strong shears due to critical latitude effects. In particular, the critical latitude of the M_2 tide coincides with Parry Channel. Consequently, the clockwise component of the tide has thick surface and bottom boundary layers resulting in mixing in the interior [*Prandle*, 1982]. Tides can also induce persistent vertical motions through enhanced Ekman pumping and stretching of relative vorticity. *Luneva et al*. [2015] demonstrated that these motions can result in penetration of Atlantic Water to the surface in the Arctic Ocean. These authors also note the strong potential for these motions in the Archipelago, but their model is too coarse to sufficiently resolve internal tidal effects in this shallower region.

Quantitatively, tidally induced mixing may be as strong or stronger than the mixing accounted for in this study. For example, *Kagan et al*. [2010] calculated the depth-average vertical diffusivity due to internal-tide-induced mixing from a finite element model and found it to be 1–10$\times$10^{-5} m^2 s^{-1} throughout much of the Archipelago. Even larger values occur within Lancaster Sound where the tidal energy flux is largest [*Chen et al*., 2009]. This range of diffusivities is comparable to the inverse estimates derived here. Note, however, that *Kagan et al*. [2010] neglect interaction between internal-tide-induced turbulence and other turbulence.

Despite the influence of tides, tideless simulations are likely to remain prevalent given that many contemporary studies are focused on seasonal and interannual variability. It is therefore worth investigating whether reasonable conclusions regarding mixing can be derived from this model and by generalization those similar. Without tides, energy for mixing must come from either atmospheric forcing or the mean flow.

5.2. Evaluating the Inverse Estimates

Direct comparison between observations with the mixing rates derived here is not possible. Only a few dedicated mixing observations are available in the literature and each of these contains only a single site. Nevertheless, we attempt a comparison to at least ensure simulated mixing rates are in the ballpark of observations.

Using turbulence instrument clusters in central Barrow Strait but within 10 km of a small island and shoal, *Crawford et al*. [1999] measured hourly averaged diffusivities well below the near-surface halocline of $10^{-5}-10^{-4}$ m^2 s^{-1} with occasional spikes up to 10^{-3} m^2 s^{-1}. The lower end of this range of values is consistent with Figure 10a. We would not expect our results to display the larger diffusivities observed as we derive values averaged over 1 month and over a large area. Indeed, elevated mixing often arises due to events with hourly timescales. For example, *Marsden et al*. [1994a] observed dissipation rates south of Cornwallis Island of 10^{-6} m^2 s^{-3} associated with finite-amplitude internal waves. However, these events typically occurred only once per day and lasted only 1–2 h. As *Marsden et al*. [1994a] focused on near-surface events, we do not compare our estimated dissipation rate with their observations.

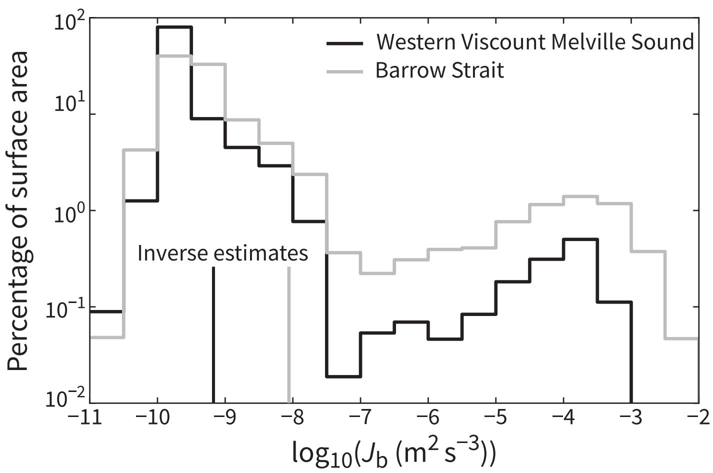

Figure 11. The distribution of buoyancy flux (J_b) on the σ_θ=27.0 kg m^{-3} isopycnal surface within the regions displaying the weakest and strongest mixing in our analysis. For the respective regions, the area-weighted histograms were created using 5 day means of diffusivity and density in grid cells vertically straddling the isopycnal surface.

To establish a better picture of the extent of enhanced mixing predicted by our model, histograms of buoyancy flux for individual grid cells were calculated (Figure 11). These are based on the density field and the diffusivity, the latter being depending on the TKE (section 2). Like other outputs, 5 day means of diffusivity were recorded. Two of the six regions are shown: western Viscount Melville Sound and Barrow Strait. The histograms are calculated from output using the whole 9 years of simulation, and to make their values comparable to earlier figures we use only cells straddling the σ_θ=27.0 kg m^{-3} isopycnal. For both sections, 80–90% of buoyancy flux values are $<10^{-9}$ m^{-2} s^{-3}. Given there is a minimum cut off for K of 10^{-6} m^{-2} s^{-1} and N^2 is typically 10^{-4} s^{-2}, this implies that most of the deep water column is, on 5 day timescales, relatively tranquil; there is insignificant shear to promote buoyancy well above low background values. However, there exists a small set of values with large buoyancy fluxes. The proportion of the water exhibiting these high buoyancy fluxes differs for the two sections shown: buoyancy fluxes exceeding 10^{-7} m^{-2} s^{-3} make up 1.4% of the total for western Viscount Melville Sound, but 6% of the total for Barrow Strait. Both histograms display a local peak at $\log_{10}(J_b)=-4$ because of the convective adjustment scheme in which a vertical diffusivity is set to 10^1 m^2 s^{-1} in unstable regions (section 2). Large buoyancy fluxes, despite their low frequency, contribute significantly to the total buoyancy flux. For example, only 10% of values in either histogram are greater than their respective inverse estimate.

Ultimately, by comparing our estimates to the limited existing observations within the Archipelago and in other regions (section 4.3), we are only able to state there is nothing that appears to notably contradict the values we obtained. Numerically, our values are the expected order of magnitude, but it is unclear whether this represents model skill or is merely attributed to using realistic values for inputs such as the minimum diffusivity. For that reason, it is arguably more useful to investigate whether the spatial variation we derived is reasonable.

5.3. Where Is Water Mass Modification Occurring?

Within the Archipelago, most modification appears to occur on the eastern side (Barrow Strait, Queens Channel, and Lancaster Sound); Figures 7, 8 and 10 suggest stronger mixing in these regions. Given the minimal flux through Queens Channel, however, it plays a lesser role in the total water mass transformation.

Given its location and topography, it is not surprising that we observed Barrow Strait to be a key region. The western edge of the region contains the shallowest (125 m) sill within Parry Channel, through which much of the total flux passes. Further, this region plays host to a number of different water masses, such as those from the southern Beaufort Sea, northeastern Canadian Basin, and Baffin Bay [*de Lange Boom et al.*, 1987].

The map of surface density in Figure 2 agrees qualitatively with our findings of stronger mixing in the eastern Archipelago. Strong lateral density gradients can indicate strong vertical mixing if it is assumed that the mixing causes water masses that are otherwise at depth to outcrop at the surface. As expected, the strongest gradients occur within Barrow Strait, and moderate gradients occur in Queens Channel and Lancaster Sound. Conversely, surface density is relatively constant on the western side of the Archipelago where smaller diffusivities were derived. Equivalent maps to that in Figure 2 but at various depths were created and showed similar patterns of horizontal gradients.

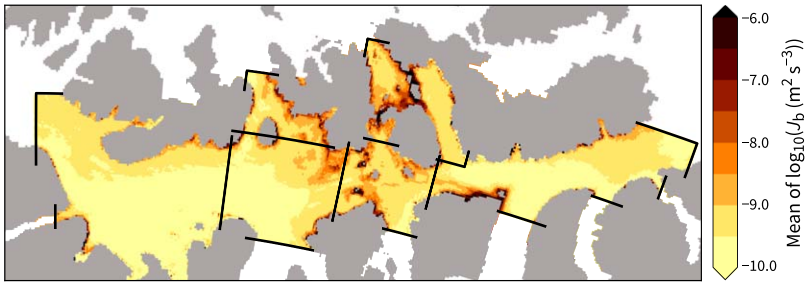

Figure 12. Mean buoyancy flux evaluated on the $\sigma_\theta = 27.0$ kg m^{-3} isopycnal surface diagnosed from the model's TKE closure scheme and density field. At each horizontal location, the value shown represents the temporal mean over the 9 years of simulation for grid cells vertically straddling the isopycnal surface. The log of $J_b = KN^2$ was calculated before the mean was taken.

Observed temperature profiles provide further support for the spatial pattern of mixing we have derived. As noted by *de Lange Boom et al*. [1987], temperature maxima and minima have been observed in the western Archipelago, but these features are smoothed away by the upward mixing of heat. Consequently they are less visible in profiles in the eastern Archipelago or Central Sills Area.

5.4. Identifying Mixing Hot Spots

Analyzing water mass changes across large volumes is necessary for understanding the fate of water moving through the volume (e.g., Figure 9). However, it provides no indication of whether the averaged mixing is spread over the volume or the result of small hot spots. To address this, Figure 12 displays mean buoyancy flux calculated using the model's diffusivity and density fields for water of density σ_θ=27.0 kg m^{-3}. The values shown are the temporal average of $\log_{10}(J_b)$. This quantity is intended as a simple measure to highlight where hot spots exist. However, it is important to reiterate a point mentioned in section 4.3: significant portions of the Archipelago may be insufficiently deep for parts of the years to host 27.0 kg m^{-3} water.

Not surprisingly, hot spots of mixing typically occur in shallower regions (see Figure 1c). The converse, however, is not always true: there exist shallow regions without elevated mixing. Hot spots of particular note are those near the centers of the Barrow Strait and Queens Channel regions. As well as being shallow, both of these areas contain small islands that further constrict the flow. Note also that despite the lack of tides in our simulation, Figure 12 displays strong similarities with a map of the expected strength of tidal mixing [see *Hannah et al*., 2009, Figure 7].

Figure 12 also helps understand the fate of water in Lancaster Sound. As described in section 3.1, the component fluxes into and out of Lancaster Sound at its eastern entrance are several times larger than the fluxes elsewhere in the Archipelago (Figure 4b). Knowing only this, one may expect this region to display the strongest mixing. However, this is not the case: average buoyancy fluxes in Lancaster Sound are similar to those in Barrow Strait and Queens Channel. The stronger fluxes appear to be counteracted by the relative lack of mixing hotspots as shown by the broad regions of low mixing values throughout the Sound.

6. Conclusion

Simple partitioning of the Canadian Arctic Archipelago into six adjoining regions demonstrates that significant differences in diapycnal diffusivity exist. Flow in the western half is comparatively tranquil, so much of the transformation of water during its transit between the Arctic and North Atlantic occurs in the eastern half. Regardless of the metric used to quantify mixing, these spatial differences were consistently displayed. The strongest mixing is attributed to the result of sills in Queens Channel and Barrow Strait. These findings suggest that the interaction of flow with bottom topography is a key feature of models seeking to accurately simulate the dynamics in the Archipelago. Indeed, further study is needed on mixing rates within topographically complex channels of the Archipelago to understand their role beyond their capacity to, say, carry a freshwater flux, which is often implied as their only important role.

With respect to temporal variation, mixing strength peaks either once or twice a year depending on the region. The largest peaks correspond to the months of peak volume flux, which typically occur in the first months of the year in our simulation. Minor peaks also occur during late summer, the time of both minimum ice coverage and strongest toward-Arctic flow.

The numerical values of diffusivity, derived here using inverse estimates, appear reasonable. However, given the lack of tides in our simulation, we expect our values to underestimate the total mixing. Regional averages for the eastern Archipelago were typically $10^{-5}-10^{-4}$ m^2 s^{-1}. Within the Archipelago, however, there is a shortage of existing mixing rate estimates with which to compare; point observations at single sites or mooring across channels are useful, but many more are needed to allow regional extrapolations. Alternatively, targeted, high-resolution observations of local processes along a channel or over a sill could help quantify and characterize the nature of mixing on scales beyond the resolution of existing observations or models. This could be complemented by process-oriented modeling with tides that enables assessment of the relative importance of mixing phenomena such as internal wave breaking, internal hydraulic jumps and shear instabilities.

Acknowledgments
The authors would like to thank Humfrey Melling and Bill Williams for helpful discussion as this work took shape and two anonymous reviewers whose feedback helped improve this work. Temperature and salinity fields used to construct Figure 2 were provided by Nicolai Kliem. Atmospheric forcing data were provided by Greg Smith of Environment and Climate Change Canada. Initial conditions and open boundary conditions were provided by MERCATOR France. Further information about the ANHA12 model configuration is available at http://knossos.eas.ualberta.ca/xianmin/anha/index.html. Data in a reduced form and scripts used to create figures are available at http://web.uvic.ca/~hugke729/.

References

Beckmann, A., and R. Döscher (1997), A method for improved representation of dense water spreading over topography in geopotential-coordinate models, *J. Phys. Oceanogr.*, *27*, 581–591, doi:10.1175/1520-0485(1997)027<0581:AMFIRO>2.0.CO;2.

Carmack, E., F. McLaughlin, M. Yamamoto-Kawai, M. Itoh, K. Shimada, R. Krishfield and A. Proshutinsky (2008), Freshwater storage in the northern ocean and the special role of the Beaufort Gyre, in *Arctic-Subarctic Ocean Fluxes: Defining the Role of the Northern Seas in Climate*, edited by R. R. Dickson, J. Meincke, and P. Rhines, pp. 145–169, Springer, Dordrecht, Netherlands, doi:10.1007/978-1-4020-6774-7_8.

Carmack, E. C., et al. (2016), Freshwater and its role in the Arctic Marine System: Sources, disposition, storage, export, and physical and biogeochemical consequences in the Arctic and global oceans, *J. Geophys. Res.*, *121*, 675–717, doi:10.1002/2015JG003140.

Chen, C., G. Gao, J. Qi, A. Proshutinsky, R. C. Beardsley, Z. Kowalik, H. Lin and G. Cowles (2009), A new high-resolution unstructured grid finite volume Arctic Ocean model (AO-FVCOM): An application for tidal studies, *J. Geophys. Res.*, *114*, C08017, doi:10.1029/2008JC004941.

Crawford, G., L. Padman and M. McPhee (1999), Turbulent mixing in Barrow Strait, *Cont. Shelf Res.*, *19*, 205–245, doi:10.1016/S0278-4343(98)00086-7.

de Lange Boom, B. R., H. Melling and R. A. Lake (1987), Late winter hydrography of the Northwest Passage: 1982, 1983 and 1984, *Can. Tech. Rep. Hydrogr. Ocean Sci.*, *79*, 165.

Ferron, B., H. Mercier, K. Speer, A. Gargett and K. Polzin (1998), Mixing in the Romanche Fracture Zone, *J. Phys. Oceanogr.*, *28*, 1929–1945, doi:10.1175/1520-0485(1998)028<1929:MITRFZ>2.0.CO;2

Ferry, N., L. Parent, G. Garric, B. Barnier, N. C. Jourdain and the Mercator Ocean Team (2010), Mercator global eddy permitting ocean reanalysis GLORYS1V1: Description and results, *Mercator Ocean Q. Newsl.*, *36*, 15–27.

Fichefet, T., and M. A. Morales Maqueda (1997), Sensitivity of a global sea ice model to the treatment of ice thermodynamics and dynamics, *J. Geophys. Res.*, *102*(C6), 12,609–12,646, doi:10.1029/97JC00480.

Fissel, D. B., D. Lemon and D. N. Knight (1984), An oceanographic survey of the Canadian Arctic Archipelago March 1983, *Tech. Rep. 16*, Inst. of Ocean Sci., Sidney, B. C., Canada.

Gregg, M. C., D. W. Winkel, J. A. MacKinnon and R. C. Lien (1999), Mixing over shelves and slopes, in *Hawaiian Winter Workshop on Dynamics of Oceanic Internal Gravity Waves II*, edited by P. Müller and D. Henderson, pp. 35–42, University of Hawaii, Manoa, Honolulu, HI.

Hannah, C. G., F. Dupont and M. Dunphy (2009), Polynyas and tidal currents in the Canadian Arctic Archipelago, *Arctic*, *62*(1), 83–95, doi:10.14430/arctic115.

Hogg, N., P. Biscaye, W. Gardner and W. J. Schmitz Jr. (1982), On the transport and modification of Antarctic Bottom Water in the Vema Channel, *J. Mar. Res.*, *40*, suppl., 231–263.

Houssais, M.-N., and C. Herbaut (2011), Atmospheric forcing on the Canadian Arctic Archipelago freshwater outflow and implications for the Labrador Sea variability, *J. Geophys. Res.*, *116*, C00D02, doi:10.1029/2010JC006323.

Hu, X., and P. G. Myers (2014), Changes to the Canadian Arctic Archipelago sea ice and freshwater fluxes in the twenty-first century under the Intergovernmental Panel on Climate Change A1B climate scenario, *Atmos. Ocean*, *52*(4), 331–350, doi:10.1080/07055900.2014.942592.

Ivey, G. N., K. B. Winters and J. R. Koseff (2008), Density stratification, turbulence, but how much mixing?, *Annu. Rev. Fluid Mech.*, *40*, 169–184, doi:10.1146/annurev.fluid.39.050905.110314.

Kagan, B. A., E. V. Sofina and A. A. Timofeev (2010), On diapycnal mixing induced by internal tidal waves in the Arctic Ocean, *Izvestiya Atmos. Oceanic Phys.*, *46*, 224–231, doi:10.1134/S0001433810020106.

Kliem, N., and D. A. Greenberg (2003), Diagnostic simulations of the summer circulation in the Canadian Arctic Archipelago, *Atmos. Ocean*, *41*(4), 273–289, doi:10.3137/ao.410402.

Klymak, J. M., and M. C. Gregg (2004), Tidally generated turbulence over the Knight Inlet Sill, *J. Phys. Oceanogr.*, *34*, 1135–1151, doi:10.1175/1520-0485(2004)034<1135:TGTOTK>2.0.CO;2.

Lindsay, R. (2013), *Unified Sea Ice Thickness Climate Data Record Collection Spanning 1947-2012, Version 1*, National Snow and Ice Data Center (NSIDC), Boulder, Colo., doi:10.7265/N5D50JXV.

Lu, Y., R. G. Lueck and D. Huang (2000), Turbulence characteristics in a tidal channel, *J. Phys. Oceanogr.*, *30*, 855–867, doi:10.1175/1520-0485(2000)030<0855:TCIATC>2.0.CO;2.

Lu, Y., S. Higginson, S. Nudds, S. Prinsenberg and G. Garric (2014), Model simulated volume fluxes through the Canadian Arctic Archipelago and Davis Strait: Linking monthly variations to forcing in different seasons, *J. Geophys. Res. Oceans*, *119*, 1927–1942, doi:10.1002/2013JC009408.

Luneva, M. V., Y. Aksenov, J. D. Harle and J. T. Holt (2015), The effects of tides on the water mass mixing and sea ice in the Arctic Ocean, *J. Geophys. Res. Oceans*, *120*, 6669–6699, doi:10.1002/2014JC010310.

Madec, G., and the NEMO team (2008), NEMO ocean engine, *Inst. Pierre-Simon Laplace 27*, Institut Pierre-Simon Laplace, France.

Marsden, R., R. Ingram and L. Legendre (1994a), Currents under land-fast ice in the Canadian Arctic Archipelago part 2: Vertical mixing, *J. Mar. Res.*, *52*, 1037–1049, doi:10.1357/0022240943076812.

Marsden, R., R. Paquet and R. Ingram (1994b), Currents under land-fast ice in the Canadian Arctic Archipelago part 1: Vertical velocities, *J. Mar. Res.*, *52*, 1017–1036, doi:10.1357/0022240943076795.

McGeehan, T., and W. Maslowski (2012), Evaluation and control mechanisms of volume and freshwater export through the Canadian Arctic Archipelago in a high-resolution pan-Arctic ice-ocean model, *J. Geophys. Res.*, *117*, C00D14, doi:10.1029/2011JC007261.

Melling, H., C. Haas and E. Brossier (2015), Invisible polynyas: Modulation of fast ice thickness by ocean heat flux on the Canadian polar shelf, *J. Geophys. Res. Oceans*, *120*, 777–795, doi:10.1002/2014JC010404.

Münchow, A., K. K. Falkner and H. Melling (2007), Spatial continuity of measured seawater and tracer fluxes through Nares Strait, a dynamically wide channel bordering the Canadian Archipelago, *J. Mar. Res.*, *65*(6), 759–788, doi:10.1357/002224007784219048.

Osborn, T. R. (1980), Estimates of the local rate of vertical diffusion from dissipation measurements, *J. Phys. Oceanogr.*, *10*(1), 83–89, doi: 10.1175/1520-0485(1980)010<0083:EOTLRO>2.0.CO;2.

Peterson, I., J. Hamilton, S. Prinsenberg, and R. Pettipas (2012), Wind-forcing of volume transport through Lancaster Sound, *J. Geophys. Res.*, *117*, C11018, doi:10.1029/2012JC008140.

Prandle, D. (1982), The vertical structure of tidal currents, *Geophys. Astrophys. Fluid Dyn.*, *22*, 29–49, doi:10.1080/03091928208221735.

Prinsenberg, S., J. Hamilton, I. Peterson, and R. Pettipas (2009), Observing and interpreting the seasonal variability of the oceanographic fluxes passing through Lancaster Sound of the Canadian Arctic Archipelago, in *Influence of Climate Change on the Changing Arctic and Sub-Arctic Conditions*, edited by J. C. J. Nihoul and A. G. Kostianoy, pp. 125–143, Springer, Dordrecht, The Netherlands, doi:10.1007/978-1-4020-9460-6_10.

Prinsenberg, S. J., and E. B. Bennett (1987), Mixing and transports in Barrow Strait, the central part of the Northwest Passage, *Cont. Shelf Res.*, *7*(8), 913–935, doi:10.1016/0278-4343(87)90006-9.

Prinsenberg, S. J., and E. B. Bennett (1989), Transport between Peel Sound and Bar row Strait in the Canadian Arctic, *Cont. Shelf Res.*, *9*(5), 427–444, doi:10.1016/0278-4343(89)90008-3 .

Rainville, L., C. M. Lee and R. A. Woodgate (2011), Impact of wind-driven mixing in the Arctic Ocean, *Oceanography*, *24*, 136–145, doi: 10.5670/oceanog.2011.65.

Seim, H. E., and M. C. Gregg (1994), Detailed observations of a naturally occurring shear instability, *J. Geophys. Res.*, *99*(C5), 10,049–10,073, doi:10.1029/94JC00168.

Smith, G. C., F. Roy, P. Mann, F. Dupont, B. Brasnett, J. F. Lemieux, S. Laroche, and S. Bélair (2013), A new atmospheric dataset for forcing ice-ocean models: Evaluation of reforecasts using the Canadian global deterministic prediction system, *Q. J. R. Meteorol. Soc.*, *140*, 881–894, doi:10.1002/qj.2194.

Staalstrøm, A., L. Arneborg, B. Liljebladh and G. Broström (2015), Observations of turbulence caused by a combination of tides and mean baroclinic flow over a fjord sill, *J. Phys. Oceanogr.*, *45*(2), 355–368, doi:10.1175/JPO-D-13-0200.1.

Wang, Q., P. G. Myers, X. Hu and A. B. G. Bush (2012), Flow constraints on pathways through the Canadian Arctic Archipelago, *Atmos. Ocean*, *50*, 373–385, doi:10.1080/07055900.2012.704348.

Wekerle, C., Q. Wang, S. Danilov, T. Jung and J. Schröter (2013), The Canadian Arctic Archipelago throughflow in a multiresolution global model: Model assessment and the driving mechanism of interannual variability, *J. Geophys. Res. Oceans*, *118*, 4525–4541, doi:10.1002/jgrc.20330.

Whalen, C. B., L. D. Talley and J. A. MacKinnon (2012), Spatial and temporal variability of global ocean mixing inferred from Argo profiles, *Geophys. Res. Lett.*, *39*, L18612, doi:10.1029/2012GL053196.